Polarimetric SAR Features for Vehicle Detection in Natural Surroundings

Paul Connetable , Allan Aasbjerg Nielsen , Knut Conradsen , Ernst Krogager, *Life Senior Member, IEEE*, and Henning Skriver , *Member, IEEE*

Abstract—The increased amount of information measured by fully polarimetric synthetic aperture radar (SAR) give additional knowledge about ground scatterers. Making the best use of the polarimetric information is crucial for target detection, among other applications. Several representations of the data, such as polarimetric decompositions, have been proposed to summarize the information into polarimetric features. The relation between these features with physical properties of the scatterers has been studied in depth. The different approaches to target detection proposed make use of different polarimetric features and different properties of the targets. The goal of this article is twofold: 1) to give a brief review of polarimetric features usually used for target detection, and 2) to combine them optimally for vehicle detection in open fields, in large natural scenes. The study's backbone is a large airborne dataset in *X*-, *S*-, and *L*-bands, in which several flights following different flight tracks were performed around a controlled area with a dozen vehicles. At first, a univariate study is performed to evaluate the contrast provided by individual polarimetric features between vehicles and different types of natural covers. Then, optimal subsets of polarimetric features for distinguishing vehicles in open fields from natural cover are determined using random forest classifiers. The multivariate approach yielded better detection results for all wavelengths but brought more significant improvement as the wavelength increases. At the *X*-band, the total received power is one of the best predictive parameters for vehicle detection while the scattering mechanism characterization becomes more important at *S*- and *L*-bands.

Index Terms—Radar polarimetry, synthetic aperture radar (SAR), target detection.

I. INTRODUCTION

THE all-weather capabilities of synthetic aperture radars (SAR) make them excellent tools for Earth observation and area monitoring. Target detection in SAR imagery has been an important research topic since the introduction of SAR instruments [1], [2], be it to detect ships at sea or vehicles on land. Furthermore, the use of fully polarimetric SAR improves the knowledge and understanding of the covers and objects

Paul Connetable and Henning Skriver are with the National Space Institute, Technical University of Denmark, 2800 Kongens Lyngby, Denmark (e-mail: pconnetable@live.fr; hs@space.dtu.dk).

Allan Aasbjerg Nielsen and Knut Conradsen are with the Department of Applied Mathematics and Computer Science, Technical University of Denmark, DK-2800 Kongens Lyngby, Denmark (e-mail: alan@dtu.dk; knco@dtu.dk).

Ernst Krogager is with the Danish Ministry of Defense Acquisition and Logistics Organization, 2750 Ballerup, Denmark (e-mail: krogager@mil.dk).

scattering the emitted signal, which is of interest for target detection.

Constant false alarm rate (CFAR) algorithms are the most common target detection algorithms, which compare a pixel's value to its surroundings and detect statistical outliers. CFAR algorithms are usually applied to the total received power, such as in [1], [3], [4], and [5], to detect pixels with a high received power compared to their surroundings, but they can be applied to any parameter as long as its distribution on the background is known. In [6], the magnitude of an element of the coherency matrix is directly used to detect buildings and ships with a CFAR algorithm. These detection methods require a knowledge of the parameter's distribution on the background or to estimate the distribution's probability density function on the background using window kernels, such as in [7]. The idea of comparing a pixel's value to its surroundings can be extended to the covariance matrix in approaches such as [8], in which the eigenvalues of the pixel under test are compared to those obtained on its surroundings to detect ships at sea.

Other approaches to target detection consist in comparing the measured scattering vector on every pixel to a target vector representing the target's expected behavior using matched filters [9], [10], [11]. Many approaches inspired by the image analysis have also been proposed to detect targets in SAR images, such as the use of wavelet transforms [12], [13], blob detection using variance-weighted entropy [14], or detection after a first image segmentation using superpixel algorithms [15], [16]. Lately, the use of neural networks (NN) for target detection has gotten more frequent and gives excellent results [17], [18].

For any of these approaches, the choice of the polarimetric feature or features to use is fundamental to improve and optimize detection capabilities. A lot of research has focused on understanding the covariance matrix's parameters and relating physical properties of the scattering medium to the observed covariance matrix [19], [20], [21]. Several models for scattering behaviors have been developed and lead to model-based decompositions such as [22], [23], [24], which decompose the received signal into known basic scattering mechanisms.

The goal of this article is 1) to provide an overview of polarimetric decompositions and parameters regularly used in polarimetric SAR imaging for man-made structures detection, 2) to find optimal data-driven polarimetric feature combinations for distinguishing vehicles in open fields from natural elements in large nonurban scenes. This is particularly relevant in military settings, where the ability to monitor large swaths of land in

critical. An extensive dataset acquired in *X*-, *S*-, and *L*-bands containing hundreds of vehicles placed along a dirt road, ranging from cars to armored troop transports gives this study a strong basis for a statistical analysis. The target pixels are compared to natural cover pixels, also extracted from the acquired data.

The rest of this article is organized as follows: An overview of the considered polarimetric parameters is first given in Section II, with an emphasis on multilooked features. The acquired data are described in Section III; then, a univariate contrast study of the parameters between vehicles and natural covers is performed in Section IV. Finally, optimal feature subsets for target detection are derived at all wavelengths using random forest (RF) classifiers in Section V.

II. OVERVIEW OF THE POLARIMETRIC PARAMETERS

A. Representations of the Polarimetric Data

A fully polarimetric radar both transmits and receives electromagnetic waves in two orthogonal polarized planes, often the horizontal and vertical polarizations denoted as H and V, respectively. The sensor measures the relation between the transmitted and the received waves, and the measured information for each pixel is stored in the scattering matrix $\mathbf{S}$, which in the HV polarization is

$$\mathbf{S} = \begin{bmatrix} S_{\text{HH}} & S_{\text{HV}} \\ S_{\text{VH}} & S_{\text{VV}} \end{bmatrix}. \tag{1}$$

Furthermore, for a monostatic radar, $S_{\text{HV}} = S_{\text{VH}}$, and the information is kept in the scattering vector

$$\mathbf{k} = \begin{bmatrix} S_{\text{HH}} & \sqrt{2}S_{\text{HV}} & S_{\text{VV}} \end{bmatrix}^T \tag{2}$$

where the superscript ^{T} denotes the transposed. The elements of the scattering matrix and the scattering vector are referred to as single-look complex data. The speckle noise in these measurements is reduced by working with the second-order statistics, stored in the local covariance matrix $\mathbf{C}$ defined as

$$\mathbf{C} = \langle \mathbf{k}\mathbf{k}^{*T} \rangle$$

$$= \begin{bmatrix} \langle |S_{\text{HH}}|^2 \rangle & \sqrt{2}\langle S_{\text{HH}}S_{\text{HV}}^* \rangle & \langle S_{\text{HH}}S_{\text{VV}}^* \rangle \\ \sqrt{2}\langle S_{\text{HV}}S_{\text{HH}}^* \rangle & 2\langle |S_{\text{HV}}|^2 \rangle & \sqrt{2}\langle S_{\text{HV}}S_{\text{VV}}^* \rangle \\ \langle S_{\text{VV}}S_{\text{HH}}^* \rangle & \sqrt{2}\langle S_{\text{VV}}S_{\text{HV}}^* \rangle & \langle |S_{\text{VV}}|^2 \rangle \end{bmatrix} \tag{3}$$

where $\langle . \rangle$ is the local average, and the superscript * denotes the complex conjugate. Going from the scattering matrix to the covariance matrix is also known as multilooking. The trace of this matrix, also known as span, corresponds to the total received power.

The information carried in the scattering vector $\mathbf{k}$ can also be represented, notably in the Pauli basis defined as

$$\mathbf{k}_P = \frac{1}{\sqrt{2}} \begin{bmatrix} S_{\text{HH}} + S_{\text{VV}} \\ S_{\text{HH}} - S_{\text{VV}} \\ S_{\text{VH}} + S_{\text{HV}} \end{bmatrix}. \tag{4}$$

The corresponding second-order statistics matrix, the coherency matrix, is defined as

$$\mathbf{T} = \langle \mathbf{k}_P \mathbf{k}_P^{*T} \rangle. \tag{5}$$

Finally, another useful and common representation of the information contained in $\mathbf{k}$ consists in shifting the polarization basis to the circular polarization. On this basis, the two orthogonal polarizations are the right-handed polarization, denoted R, and the left-handed one, denoted L. The transformation from the linear to the circular basis is made with [25]

$$S_{\text{RR}} = (S_{\text{HH}} - S_{\text{VV}} + 2jS_{\text{HV}})/2$$

$$S_{\text{RL}} = j(S_{\text{HH}} + S_{\text{VV}})/2$$

$$S_{\text{LL}} = (S_{\text{VV}} - S_{\text{HH}} + 2jS_{\text{HV}})/2 \tag{6}$$

and the corresponding information vector created is

$$\mathbf{k}_{\text{RL}} = \begin{bmatrix} S_{\text{RR}} & \sqrt{2}S_{\text{RL}} & S_{\text{LL}} \end{bmatrix}^T. \tag{7}$$

The covariance matrix in the circular polarization denoted $\mathbf{C}_{\text{RL}}$ is defined as

$$\mathbf{C}_{\text{RL}} = \langle \mathbf{k}_{\text{RL}} \mathbf{k}_{\text{RL}}^{*T} \rangle. \tag{8}$$

The three matrices $\mathbf{C}$, $\mathbf{T}$, and $\mathbf{C}_{\text{RL}}$ carry the same information, and it is possible to go from one representation to another easily. They are all Hermitian and are mathematically similar, which means that they represent the same information under a changed basis and, therefore, share the same eigenvalues

$$\mathbf{C} = \begin{bmatrix} C_{11} & C_{12} & C_{13} \\ C_{12}^* & C_{22} & C_{23} \\ C_{13}^* & C_{23}^* & C_{33} \end{bmatrix}$$

$$\mathbf{T} = \begin{bmatrix} T_{11} & T_{12} & T_{13} \\ T_{12}^* & T_{22} & T_{23} \\ T_{13}^* & T_{23}^* & T_{33} \end{bmatrix}$$

$$\mathbf{C}_{\text{RL}} = \begin{bmatrix} C_{\text{RRRR}} & C_{\text{RRRL}} & C_{\text{RRLL}} \\ C_{\text{RRRL}}^* & C_{\text{RLRL}} & C_{\text{RLLL}} \\ C_{\text{RRLL}}^* & C_{\text{RLLL}}^* & C_{\text{LLLL}} \end{bmatrix}. \tag{9}$$

B. Orientation Angle Alignment

Polarization shifts are induced by slopes in both the azimuth and range directions, as well as the orientation of objects with regard to the radar line of sight [25]. This is of particular importance for dihedral scatterers, which give a strong double-bounce return when they are orthogonal with the radar illumination but for which the cross-polarized return $|S_{\text{HV}}|^2$ increases instead when their orientation is tilted, as observed in [26] among others. As some polarimetric parameters used in this study are based on polarimetric decompositions, the use of a unified methodology that removes the influence of objects' orientations is needed to compare measurements. This is achieved by applying to each covariance matrix a rotation by the angle, which minimizes the cross-polar return $\langle |S_{\text{HV}}|^2 \rangle$, also known as the orientation angle. The rotation of the scattering matrix by any angle θ is achieved

through [25]

$$\mathbf{S}(\theta) = \begin{bmatrix} \cos(\theta) & \sin(\theta) \\ -\sin(\theta) & \cos(\theta) \end{bmatrix} \mathbf{S} \begin{bmatrix} \cos(\theta) & -\sin(\theta) \\ \sin(\theta) & \cos(\theta) \end{bmatrix}. \quad (10)$$

It follows that the rotation of the covariance matrix by angle θ has a simple expression

$$\mathbf{C}(\theta) = \mathbf{U}(\theta)\mathbf{C}\mathbf{U}(\theta)^T \quad (11)$$

with

$$\mathbf{U}(\theta)$$
$$= \frac{1}{2} \begin{bmatrix} 1 + \cos(2\theta) & \sqrt{2}\sin(2\theta) & 1 - \cos(2\theta) \\ -\sqrt{2}\sin(2\theta) & 2\cos(2\theta) & \sqrt{2}\sin(2\theta) \\ 1 - \cos(2\theta) & -\sqrt{2}\sin(2\theta) & 1 + \cos(2\theta) \end{bmatrix}. \quad (12)$$

This transformation keeps all the properties of the covariance matrix and the obtained matrix $\mathbf{C}(\theta)$ is mathematically similar to the original matrix $\mathbf{C}$. The local orientation angle estimate is found through the circular polarization algorithm as described in [25] and [27]. It is a robust estimator with low noise levels compared to the other algorithms presented. It corresponds to the solution found in [26] for cross-polarization return minimization, which is

$$\tan 4\hat{\theta} = \frac{-4\mathrm{Re}(\langle (S_{\mathrm{HH}} - S_{\mathrm{VV}})S_{\mathrm{HV}}^*\rangle)}{4\langle|S_{\mathrm{HV}}|^2\rangle - \langle|S_{\mathrm{HH}} - S_{\mathrm{VV}}|^2\rangle}$$
$$= \frac{-2\mathrm{Re}(T_{23})}{T_{33} - T_{22}}. \quad (13)$$

The orientation angle alignment is applied to all the data in this article, by applying a rotation of angle $-\hat{\theta}$ to each covariance matrix.

C. Parameters Based on Eigenvector/Eigenvalue Decompositions

1) H/A/α Decomposition: The second-order matrices are Hermitian, which means that they share the same eigenvalues $\lambda_1, \lambda_2, \lambda_3 \in \mathbb{R}^{+3}$, noted in order of decreasing values without loss of generality. The well-known entropy/anisotropy/α decomposition introduced by Cloude and Pottier in [19] relies on an eigenvalue/eigenvector decomposition of the coherency matrix $\mathbf{T}$ such that

$$H = -\sum_{i=1}^{3} P_i \log(P_i) \quad \text{with} \quad P_i = \frac{\lambda_i}{\sum_{k=1}^{3} \lambda_k}$$

$$\bar{\alpha} = \sum_{i=1}^{3} P_i \alpha_i$$

$$A = \frac{\lambda_2 - \lambda_3}{\lambda_2 + \lambda_3} \quad (14)$$

where α_i are obtained from the first element of each eigenvector.

2) Other Similarity Invariants: Other parameters of interest can be obtained through the eigenvalues of the second-order matrices. Here, $\mathbf{\Gamma}$ denotes a general second-order matrix since the different representations are mathematically similar. Most notably, the parameters of interest here and studied more in depth

in [28] are, respectively, the span, the determinant, and Frobenius norm

$$Tr(\mathbf{\Gamma}) = \lambda_1 + \lambda_2 + \lambda_3$$
$$\det(\mathbf{\Gamma}) = \lambda_1 \lambda_2 \lambda_3$$
$$||\mathbf{\Gamma}||_F^2 = \lambda_1^2 + \lambda_2^2 + \lambda_3^2. \quad (15)$$

Notably, the span corresponds to total received power and has been particularly central in target detection: An extensive review of these works is presented in [1], and some applications examples in [3], [7], [29], and [30].

3) Degree of Polarization: The degree of polarization (DoP) is another well-known and widely used polarimetric parameter, which has proven its interest in applications such as oil-spill, ship, or oil-rig detection at sea [31], as well as land cover classification [32]. We recall its generalized expression given by Barakat in [33]. For fully polarimetric data, the DoP is given by

$$\mathcal{P}_3 = \left(1 - 27\frac{\det(\mathbf{\Gamma})}{Tr(\mathbf{\Gamma})^3}\right)^{1/2} \quad (16)$$

and for dual-polarization data

$$\mathcal{P}_2 = \left(1 - 4\frac{\det(\mathbf{\Gamma}_2)}{Tr(\mathbf{\Gamma}_2)^2}\right)^{1/2} \quad (17)$$

where $\mathbf{\Gamma}_2$ is the 2×2 covariance matrix (or similar representations) obtained for a given dual-polarization choice. To analyze the relative information contained in the different dual-polarization modes, we denote $\mathbf{k}_2$ such that $\mathbf{\Gamma}_2 = \langle \mathbf{k}_2 \mathbf{k}_2^{*T}\rangle$ and keep the following parameters:

$$\mathcal{P}_H \text{ for } \mathbf{k}_2 = [S_{\mathrm{HH}} \quad S_{\mathrm{HV}}]^T$$
$$\mathcal{P}_V \text{ for } \mathbf{k}_2 = [S_{\mathrm{HV}} \quad S_{\mathrm{VV}}]^T$$
$$\mathcal{P}_{HV} \text{ for } \mathbf{k}_2 = [S_{\mathrm{HH}} \quad S_{\mathrm{VV}}]^T. \quad (18)$$

4) Nonmodel-Based Three Components Decomposition: Dey et al. [32] propose a roll-invariant three-component decomposition based on the use of the DoP. For fully polarimetric data, the backbone of the decomposition relies on the definition of the angle θ_{fp} such that

$$\tan(\theta_{\mathrm{fp}}) = \frac{\mathcal{P}_3 \, Tr(\mathbf{\Gamma})(T_{11} - T_{22} - T_{33})}{T_{11}(T_{22} + T_{33}) + \mathcal{P}_3^2 Tr(\mathbf{\Gamma})^2}. \quad (19)$$

The decomposition's double-bounce, single-bounce, and volume scattering power are obtained, respectively, as

$$P_{\mathrm{db,fp}} = \frac{\mathcal{P}_3 \, Tr(\mathbf{\Gamma})}{2}(1 - \sin(2\theta_{\mathrm{fp}}))$$
$$P_{\mathrm{s,fp}} = \frac{\mathcal{P}_3 \, Tr(\mathbf{\Gamma})}{2}(1 + \sin(2\theta_{\mathrm{fp}}))$$
$$P_{\mathrm{v,fp}} = Tr(\mathbf{\Gamma})(1 - \mathcal{P}_3). \quad (20)$$

D. Polarimetric Decompositions

Model-based decompositions take a different approach that is to model the return from known structures and to decompose the received signal as a sum of these scattering elements. This

TABLE I
SCATTERING MECHANISMS AND THEIR CORRESPONDING CANONICAL SCATTERERS

Scattering component	Scattering vector in the Pauli basis	Canonical target scattering type
$S_1 = S_{HH}$	$\mathbf{q}_1 = \begin{bmatrix} 1 & 1 & 0 \end{bmatrix}^T / \sqrt{2}$	Horizontal dipole
$S_2 = S_{VV}$	$\mathbf{q}_2 = \begin{bmatrix} 1 & -1 & 0 \end{bmatrix}^T / \sqrt{2}$	Vertical dipole
$S_3 = \sqrt{2} S_{HV}$	$\mathbf{q}_3 = \begin{bmatrix} 0 & 0 & 1 \end{bmatrix}^T$	Rotated dihedrals, rotated dipoles, volume scattering
$S_4 = (S_{HH} + S_{VV})/\sqrt{2}$	$\mathbf{q}_4 = \begin{bmatrix} 1 & 0 & 0 \end{bmatrix}^T$	Sphere, rough terrain, trihedral scatterers
$S_5 = (S_{HH} - S_{VV})/\sqrt{2}$	$\mathbf{q}_5 = \begin{bmatrix} 0 & 1 & 0 \end{bmatrix}^T$	Dihedral scatterers
$S_6 = (S_{HH} - S_{VV} + 2jS_{HV})/2$	$\mathbf{q}_6 = \begin{bmatrix} 0 & 1 & j \end{bmatrix}^T / \sqrt{2}$	Left-wound helix
$S_7 = (-S_{HH} + S_{VV} + 2jS_{HV})/2$	$\mathbf{q}_7 = \begin{bmatrix} 0 & -1 & j \end{bmatrix}^T / \sqrt{2}$	Right-wound helix
$S_8 = (S_{HH} + S_{VV} + 2S_{HV})/2$	$\mathbf{q}_8 = \begin{bmatrix} 1 & 0 & 1 \end{bmatrix}^T / \sqrt{2}$	Rotated horizontal dipole
$S_9 = (S_{HH} + S_{VV} - 2S_{HV})/2$	$\mathbf{q}_9 = \begin{bmatrix} 1 & 0 & -1 \end{bmatrix}^T / \sqrt{2}$	Rotated vertical dipole

approach was first introduced by Huynen in [34] and later developed further in several works. This part provides a short overview and explanation of some of these decompositions, from which some polarimetric parameters are extracted.

1) Scattering Degree of Preference: As an extension to the decomposition proposed by Huynen in [34] and Li and Zhang [35] identified nine scattering mechanisms, presented in Table I to analyze the polarimetric response of a target. These nine mechanisms can be used to analyze if there is a preferred scattering from vehicles and can serve as a basis to select an appropriate scattering mechanism to identify in polarimetric target detectors such as [10]. Both the direct use of the local average of the power of the component $\langle |S_i|^2 \rangle$ and the use of the scattering degree of preference (SDOP) defined for every dichotomy in [35] as

$$\text{SDOP}_i = \frac{||\mathbf{T}\mathbf{q}_i||_F^2}{\mathbf{q}_i^{*T} \mathbf{T} \mathbf{q}_i \text{Tr}(\mathbf{T})} \qquad (21)$$

are investigated.

2) Coherent Decompositions: Coherent decompositions are the polarimetric decompositions applied on the single-look complex data contained in the scattering matrix $\mathbf{S}$, which model pointlike scatterers. Three such decompositions are described and used here, namely the Pauli decomposition, the Corr decomposition described in [36], and the Krogager decomposition [37]. The Pauli and Corr decompositions are used as the alternative bases used to, respectively, form the coherency matrix $\mathbf{T}$ and the covariance matrix in the circular polarization $\mathbf{C}_{RL}$. The multilooked version of its parameters is, therefore, simply found as the diagonal elements of these matrices.

The decomposition proposed by Krogager in [24], also known as the sphere–diplane–helix (SDH) decomposition, decomposes the scattering power into three components, which can be found as follows [37]:

$$k_s = |S_{RL}|$$
$$k_h = \min(|S_{LL}|, |S_{RR}|)$$
$$k_d = ||S_{RR}| - |S_{LL}||. \qquad (22)$$

3) Incoherent Decompositions: Incoherent decomposition focuses on modeling scattering mechanisms under the covariance matrix form, which is most suitable for distributed scattering. Four incoherent decompositions are included in this study and are shortly described. The methodology to derive the scattering powers from these decompositions is not recalled here but is well-explained in their respective publications. The

TABLE II
NOTATIONS FOR THE SCATTERING POWERS DERIVED FROM THE FOUR
INCOHERENT DECOMPOSITIONS PRESENTED

	Volume scattering	Double-bounce scattering	Single-bounce scattering	Helix scattering
Freeman and Durden	$P_{v,\text{DF}}$	$P_{db,\text{DF}}$	$P_{sb,\text{DF}}$	/
Yamaguchi	$P_{v,\text{Ya}}$	$P_{db,\text{Ya}}$	$P_{sb,\text{Ya}}$	$P_{h,\text{Ya}}$
Van Zyl	$P_{v,\text{VZ}}$	$P_{db,\text{VZ}}$	$P_{sb,\text{VZ}}$	/
NNED	$P_{v,\text{NNED}}$	$P_{db,\text{NNED}}$	$P_{sb,\text{NNED}}$	/

notations related to the scattering powers derived from these decompositions are listed in Table II.

The Freeman and Durden three-component decomposition introduced in [22] explains the scattering as the weighted sum of volume, rough surface, and double-bounce scattering, each obtained through mathematical modeling under the covariance matrix form.

The four-component decomposition proposed by Yamaguchi et al. in [23] is a direct improvement to the Freeman and Durden decomposition, by adding the helix scattering as a fourth element in the decomposition, and an improvement to the modeling of volume scattering.

The decomposition proposed by Van Zyl in [38] is a bridge between data-driven decompositions such as the entropy/alpha and the model-based decompositions. It shows that under the assumption of reflection symmetry, the scattering mechanisms obtained with the matrix eigenvectors correspond to single-bounce, double-bounce, and a mechanism analogous to volume scattering.

Finally, the nonnegative eigenvalue decomposition (NNED), introduced in [39], is a further refined approach to incoherent decomposition, using together some modeling and the eigenvalue decomposition from [38]. For any volume scattering model $\mathbf{C}_{\text{model}}$, the decomposition aims to find the maximum volume scattering power, which can be derived while keeping the rest of the powers positive. Afterward, the Van Zyl decomposition [38] can be applied to the remainder matrix, to find the double-bounce and single-bounce scattering powers.

E. Other Polarimetric Parameters of Interest

Finally, this section presents additional useful polarimetric parameters proposed in the literature, which are also interesting in this target detection setting.

1) Symmetry Parameter: The first parameter considered here is the symmetry parameter, noted δ_e, and was proposed in [40] as a way to identify scatterer orientations in a medium. The use of this parameter was reported thereafter and in other works such as [41] to compare and analyze the structure of different types of natural covers. It was particularly relevant to distinguish different types of forest canopies and sea ice types. Its expression is given by

$$\delta_e = \frac{C_{22}}{C_{11}(1 - |C_{13}|/\sqrt{C_{11}C_{33}})}. \qquad (23)$$

The values δ_e are typically small for scatterers with a structure that corresponds to vehicles and are higher for other types of natural scattering. This is why the values of δ_e^{-1} are reported in this work.

2) Reflection Symmetry: Natural media, as opposed to man-made structures and objects, is often reflection symmetric. In the coherency matrix stemming from a reflection symmetric scattering, T_{13}, T_{23}, and their complex conjugates are null [42]. These properties motivated several approaches such as [6], [43], and [44] to investigate the use of $|T_{23}|$ to detect buildings embedded in the natural background and ships at sea, with convincing results. It corresponds to the helix power obtained with the decomposition proposed by Yamaguchi et al. [23] once the orientation angle alignment has been performed on the matrices and is already included in the feature list under study. $|T_{13}|$ is included in this work as well, as it does not highlight the same scattering mechanics.

3) Complex Correlation Between the HH and VV Channels: The complex correlation coefficient between the HH and VV channels is denoted

$$\rho_{\text{HHVV}} = \frac{C_{13}}{\sqrt{C_{11}C_{33}}} = |\rho_{\text{HHVV}}|e^{j\varphi} \qquad (24)$$

where φ is the correlation's phase. The copolar phase difference $\phi_c = \phi_{\text{HH}} - \phi_{\text{VV}}$ carries valuable information on the scattering. To reduce speckle noise, the considered phase φ is extracted directly from the correlation coefficient. This phase difference has been used for oil-spill detection in works such as [31], [45], [46], [47] and analysis of crop fields [48], and its distribution is well known. The values of this phase difference are known to be dependent on the conductivity and dielectric properties of the material scattering the electromagnetic wave [49], which can be useful for detecting metallic scatterers, such as in [50].

For target detection, the most interesting values of φ lay far from 0, regardless of the sign. To make use of this property, the following transformation is applied to the phase [31]:

$$\mathcal{B}_\varphi = \frac{1 - \cos(\varphi)}{2}. \qquad (25)$$

While less relevant for vehicle detection, the magnitudes $|\rho_{\text{HHVV}}|$, $1 - |\rho_{\text{HHVV}}|$, and $|C_{13}|$ are included in the study to assess their potential contribution to this topic. Finally, unlike the copolar phase difference, the cross-polar phase differences, between the HH and HV channels and the VV and HV channels are distributed uniformly on natural covers [31] and, therefore, are not included in this study.

TABLE III
SYSTEM PARAMETERS OF THE F-SAR INSTRUMENT, IN METERS

	Pixel size azimuth (m)	Pixel size range (m)	Resolution azimuth (m)	Resolution range (m)
X-band	0.14	0.14	0.25	0.29
S-band	0.30	0.30	0.50	0.65
L-band	0.30	0.60	0.60	1.29

4) Complex Correlation Between the RR and LL Channels: The complex correlation between the RR and LL channels is denoted

$$\rho_{\text{RRLL}} = \frac{C_{\text{RRLL}}}{\sqrt{C_{\text{RRRR}}C_{\text{LLLL}}}}. \qquad (26)$$

Its magnitude $|\rho_{\text{RRLL}}|$ is well known for providing an excellent contrast between man-made structures and natural background and has been used for man-made structure and object detection [6], [49], [51]. The magnitude $|C_{\text{RRLL}}|$ is also relevant for this purpose and is included in the list of polarimetric parameters studied. The phase of ρ_{RRLL} contains information pertaining to the orientation of objects and structures compared to the radar line of sight [25], [52] and corresponds to the orientation angle correction performed in (13).

5) Polarization Maximization Synthesis: The polarization maximization synthesis (PMS) is one of the first parameters proposed to highlight man-made targets in natural background, without a priori information about the background nor the target for fully polarimetric data [53], [54]. Its expression is given by

$$\text{PMS} = Tr(\mathbf{C}) + \sqrt{(C_{11} - C_{33})^2 + 2|C_{12} + C_{23}|^2}. \qquad (27)$$

F. Special Note on Power Parameters

All the polarimetric parameters linked to the total received power, that is the trace, determinant, Frobenius norm, PMS, the power decomposition parameters, and the magnitudes $|C_{\text{HHVV}}|$ and $|C_{\text{RRLL}}|$ were transformed in the logarithmic scale. This step is taken to improve the variance standardization performed for all parameters in the multivariate analysis.

III. DATA PRESENTATION

A. Acquisition and Vehicle Description

All the data presented were acquired with the airborne F-SAR instrument from the German Aerospace Center (DLR), in *X*-, *S*-, and *L*-bands. The resolutions for all wavelengths are presented in Table III. The acquisitions were performed in June 2017 close to Oksbøl, Denmark, by DLR for the Danish Ministry of Defense Acquisitions and Logistics Organization. The weather was clear all day during the acquisitions, with low wind speeds, and it had not rained during the previous days. This study focuses on a controlled area, in which several vehicles, ranging from cars to armored personal carriers, were placed along a dirt road, and over a short grass field. A total of 24 passes including this area were performed, following 8 different tracks with different viewing and depression angles. The vehicles were also moved to assume other positions after the 13th flight. For each wavelength, a total of 297 individual vehicles were manually cropped, using all the
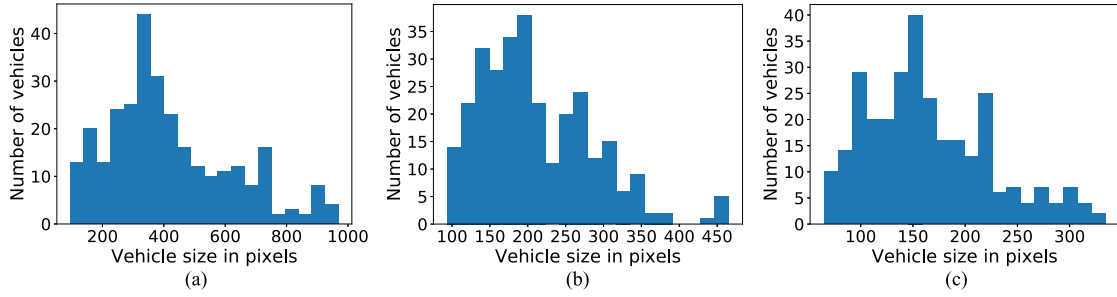
Fig. 1.   Histograms of the cropped vehicle sizes, in number of pixels. (a) *X*-band. (b) *S*-band. (c) *L*-band.

TABLE IV
MINIMUM, MAXIMUM, AND AVERAGE SIZES OF THE CROPPED VEHICLES, IN
NUMBER OF PIXELS

	Minimum size	Maximum size	Average size
X-band	95	969	417
S-band	94	465	211
L-band	65	334	165

available flights. This dataset, therefore, provides an interesting diversity of scatterers, with different azimuth orientation angles, and viewed under different depression angles. The vehicle sizes in pixels differ between the wavelengths. The maximum, minimum, and average sizes of the vehicles are indicated in Table IV, and the distributions of vehicle sizes are shown in Fig. 1.

B. Natural Cover Selection

The different polarimetric parameters' capabilities to differentiate between vehicles and natural cover is assessed by comparing the values obtained on vehicles and five types of natural cover, selected based on the available covers in the acquired imagery.

1) The first type of natural cover is a coniferous forest. In all wavelengths, the backscatter over this area is dominated by volume scattering. The intensity of the return compared to the rest of the image is higher at *S*- and *L*-bands than it is at the *X*-band. Some more double-bounce is also visible in *S*- and *L*-bands than in the *X*-band, as the wave penetrates the vegetation layer and is reflected by the tree trunks more often.
2) The second kind of cover selected is deciduous forest. The trees in this area had leaves on during the acquisition, as it was performed in June. The return over the deciduous forested areas is different from the coniferous area in the *X*-band. The intensity of the return is much higher, and surface scattering plays an important role in the backscatter. In *S*- and *L*-bands, this type of cover behaves similarly as the coniferous forested areas on which the volume scattering is predominant, with some double-bounce.
3) One of the selected natural covers selected is barren field, over which the return intensity is low at all wavelengths, and behaves as a rough surface scatterer.
4) A grass field with semitall grass. In the *X*-band, the backscatter over this field is dominated by volume scattering, with a rather high-intensity return. In both *S*- and

L-bands, the backscatter intensity from this area is low and behaves similarly as the barren field.
5) Finally, the last selected natural cover is a type of water meadow, with tall grass, reeds, and areas with shallow water. This type of cover is dominated by strong intensity double-bounce returns in *X*- and *S*-bands. In the *L*-band, the backscatter intensity is a bit lower in this area but still involves strong double-bounce returns. This area is challenging to differentiate from man-made vehicles, which makes it particularly interesting to include in the natural cover list.

The same natural areas were selected at each wavelength. Furthermore, for each wavelength, four different passes were used to select pixels over these natural covers, under two orthogonal flight directions for two different depression angles. As we expect the return from natural areas to be mostly orientation independent, this scene selection ensures that the data variation from these scenes is already fully described. This is different from the vehicle selection, which includes all vehicles from all the available flight passes. To illustrate Fig. 2 shows the intensities in the Pauli basis over the area in the *X*-band, in which yellow rectangles highlight the areas used to extract pixels from the natural cover types, with the corresponding names. Likewise, Fig. 3 shows the same area in *S*- and *L*-bands, respectively, with yellow rectangles showing the position of the natural covers.

IV. RESULTS FOR THE UNIVARIATE STUDY

A. Organization of Results

Such a large number of individual observed vehicles allows for statistical study over the vehicles rather than over the number of detected pixels for a handful of targets. This is a more robust approach to the detection problem, which also takes into account a great diversity of scenarios. The size of the dataset and the large number of parameters selected in the study also make the presentation of results more challenging. Target detectors do not need to detect all pixels from a vehicle to detect the vehicles and save the area as a region of interest. Rather, being able to detect several pixels in a close vicinity is the key to target detection, the number of pixels needed depends on the algorithms used to process the detection information.

The capacity of individual parameters to highlight vehicles as opposed to the selected natural covers is estimated by calculating the percentage of vehicles, which would be detected with a 0.1%
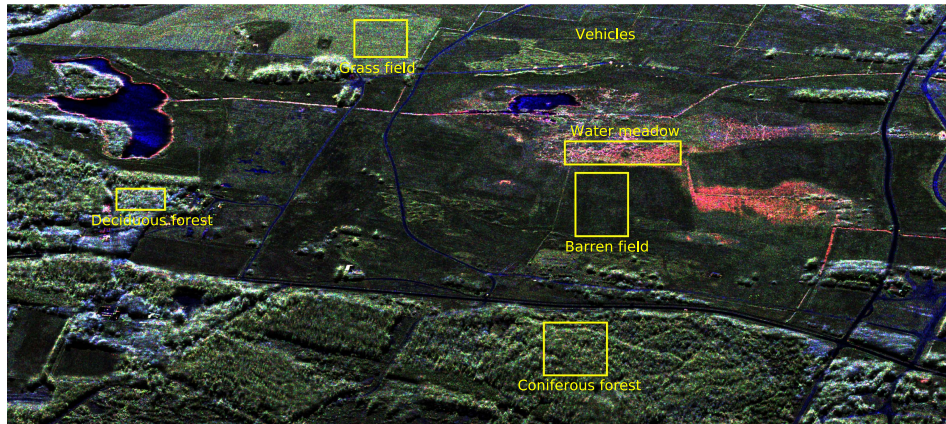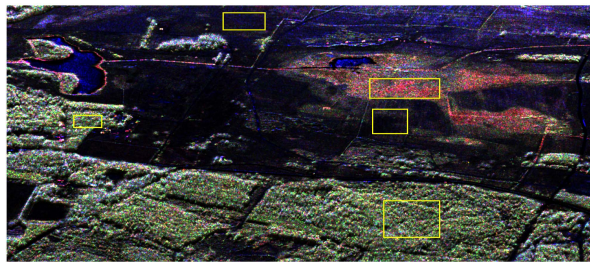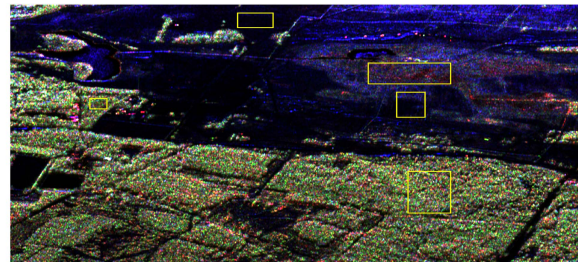
Fig. 2. X-band image of the area, in which the RGB channels correspond to $\langle|S_{HH} - S_{VV}|^2\rangle$, $2\langle|S_{HV}|^2\rangle$, and $\langle|S_{HH} + S_{VV}|^2\rangle$, respectively. Yellow rectangles delineate background areas. The vehicles, which are the targets to be detected, are toward the top of the scene.

Fig. 3. Same area as in the previous figure is shown in S- and L-bands. The RGB channels correspond to $\langle|S_{HH} - S_{VV}|^2\rangle$, $2\langle|S_{HV}|^2\rangle$, and $\langle|S_{HH} + S_{VV}|^2\rangle$, respectively, and yellow rectangles delineate the areas in which the background pixels were selected. (a) S-band. (b) L-band.

false alarm rate. The vehicle detection rule used is that at least 5% of the vehicle pixels, with a minimum of 10 pixels, are detected. For every polarimetric parameter included in the study, the 95th percentile of the parameter's distribution over each vehicle's pixels is chosen to represent the parameter's high values over the vehicle. It is then compared to the 99.9th percentile of the same polarimetric parameter over each natural cover type. For small vehicles containing less than 200 pixels, the detection rule is slightly different and requires to compare the 10th highest vehicle pixel value for the considered parameter to the natural cover's 99.9th percentile. This detection rule was chosen to scale with the vehicle sizes, and the necessity to have a minimal number of detections in the same area to not rule them out as being isolated false alarms in the filtering phase. The tables of results present the percentage of vehicles detected with the selected rule, for all polarimetric parameters and natural cover types. Though the choice of these percentiles is somewhat arbitrary, this presentation conveys the information concisely, and the relative performance of the different polarimetric parameters is still visible and interpretable. Two additional columns contain the average and the minimal value obtained on the five natural covers by the polarimetric parameters.

The results for X-, S-, and L-bands are presented, respectively, in Tables V, VI, and VII. The "average" column gives the average percentage of detected vehicles over all natural cover

types, and the "minimal value" column gives the minimum value obtained on the five natural cover types. The latter is a measure of the parameter's lowest detection capabilities; over the natural cover type, it gives the lowest contrast for vehicles. Two color codes are used to highlight noteworthy values in the tables, in a columnwise manner. In each column, all the parameters that give a result not lower than 5% of the maximal value are highlighted and represent the parameters giving the best results in each situation. These values are highlighted in blue for individual natural cover types and give an indication of the characteristics of the scattering over the specific natural cover. The values are highlighted in green following the same algorithm if they belong to the last two columns and represent a summary of the capability of each individual parameter to distinguish between vehicles and natural covers in general. The color-coding difference reflects the difference between natural cover-specific information in blue and generalization capabilities in green.

B. Results

This part summarizes some key observations from the univariate study but does not give exhaustive lists of the best performing parameters, which are already highlighted in the relevant tables. It is important to keep in mind that the spatial resolution is also known to influence the observed scattering

IEEE JOURNAL OF SELECTED TOPICS IN APPLIED EARTH OBSERVATIONS AND REMOTE SENSING, VOL. 16, 2023

TABLE V
UNIVARIATE STUDY RESULTS FOR X-BAND DATA

Terrain type / Polarimetric parameter	Coniferous forest	Deciduous forest	Barren field	Grass field	Water-Meadow	Average	Minimal value
$\mathrm{Tr}(\mathbf{\Gamma})$	87	79	100	96	83	89	79
$\mathrm{Det}(\mathbf{\Gamma})$	82	68	100	94	79	85	68
$\|\mathbf{\Gamma}\|_F^2$	87	80	100	95	82	89	80
$1-H$	52	42	34	77	54	52	34
$\bar{\alpha}$	42	54	56	49	51	50	42
A	69	63	66	70	54	65	54
$\mathcal{P}_3$	60	48	41	80	60	58	41
$\mathcal{P}_H$	73	66	60	82	65	69	60
$\mathcal{P}_V$	64	58	54	79	64	64	54
$\mathcal{P}_{\mathrm{HV}}$	44	35	33	63	42	43	33
$P_{\mathrm{db,fp}}$	82	81	100	94	71	86	71
$P_{\mathrm{sb,fp}}$	78	65	100	90	73	81	65
$P_{v,\mathrm{fp}}$	40	37	95	63	49	57	37
$\langle|S_{\mathrm{HH}}|^2\rangle$	90	82	100	94	77	89	77
$\langle2|S_{\mathrm{HV}}|^2\rangle$	47	44	96	74	52	63	44
$\langle|S_{\mathrm{VV}}|^2\rangle$	82	73	100	90	83	86	73
T_{22}	84	82	100	94	74	87	74
T_{11}	84	69	100	91	79	84	69
C_{RRRR}	75	71	99	86	70	80	70
C_{LLLL}	80	79	98	92	77	85	77
$\langle|S_8|^2\rangle$	84	66	100	92	78	84	66
$\langle|S_9|^2\rangle$	84	70	100	89	75	84	70
SDOP_1	51	44	38	72	47	51	38
SDOP_2	47	33	29	61	48	44	29
SDOP_3	18	20	18	20	17	18	17
SDOP_4	37	32	27	57	40	39	27
SDOP_5	75	80	73	72	54	71	54
SDOP_6	74	76	71	74	53	70	53
SDOP_7	70	71	73	69	56	68	56
SDOP_8	38	32	28	59	39	39	28
SDOP_9	41	34	28	57	41	40	28
$\langle k_h^2\rangle$	54	51	96	70	53	65	51
$P_{v,\mathrm{DF}}$	47	44	96	74	52	63	44
$P_{db,\mathrm{DF}}$	73	79	99	76	64	78	64
$P_{sb,\mathrm{DF}}$	83	70	99	91	73	83	70
$P_{v,\mathrm{Yama}}$	40	39	94	62	43	56	39
$P_{db,\mathrm{Yama}}$	75	79	97	79	63	79	63
$P_{sb,\mathrm{Yama}}$	88	72	100	92	73	85	72
$P_{h,\mathrm{Yama}}$	71	65	98	83	65	76	65
$P_{db,\mathrm{VZ}}$	84	84	99	91	69	85	69
$P_{sb,\mathrm{VZ}}$	82	72	100	92	74	84	72
$P_{v,\mathrm{NNED}}$	55	44	97	77	55	66	44
$P_{db,\mathrm{NNED}}$	82	83	99	88	67	84	67
$P_{sb,\mathrm{NNED}}$	85	71	99	93	72	84	71
$|\rho_{\mathrm{HHVV}}|$	39	30	26	54	41	38	26
$1-|\rho_{\mathrm{HHVV}}|$	0	0	0	0	0	0	0
$|C_{13}|$	83	71	99	89	79	84	71
$\mathcal{B}_\varphi$	9	29	23	11	10	16	9
$|\rho_{\mathrm{RRLL}}|$	86	83	84	81	63	79	63
$|C_{\mathrm{RRLL}}|$	87	87	99	92	73	88	73
δ_e	64	67	64	64	38	60	38
$|T_{13}|$	71	54	100	81	60	73	54
PMS	89	82	100	95	80	89	80

The values are the percentage of vehicles for which 5% of the vehicle's pixels, with a minimum of 10 pixels, have higher values than the 99.9th percentile of the corresponding natural cover type, for each considered polarimetric parameter.

properties [55], [56]; hence, the differences observed here cannot only be explained by different wavelengths. Since this is a forward description of experimental results, we still refer to each wavelength separately by its name. Comparing the results obtained at the three wavelengths shows a decreasing trend in the overall detection capabilities of individual polarimetric parameters, from the X-band to S- and L-bands. The highest average percentage and minimal value over the five natural cover types go from 89% and 80%, respectively, at the X-band, to 76% and 56% at the S-band, and 61% and 38% at the L-band. This does not necessarily indicate that the X-band is better suited for target detection in general but rather that the relevant information

for target detection is more spread between several features in S- and L-bands. In other words, a univariate approach appears less fitted for target detection at the L-band as compared to the X-band on this dataset. The features, which give the best generalized results over all natural cover types, and should be chosen for univariate approaches, are those giving the best average result and the highest minimal value over the five natural covers, and are, therefore, highlighted in green in these two columns.

The results for the X-band (see Table V) corroborate the observations made for the different natural covers. The total received power (span) over deciduous trees is high, and using it to detect vehicles can lead to a high amount of false alarms

TABLE VI
UNIVARIATE STUDY RESULTS FOR *S*-BAND DATA

Polarimetric parameter / Terrain type	Coniferous forest	Deciduous forest	Barren field	Grass field	Water-Meadow	Average	Minimal value
$\mathrm{Tr}(\mathbf{\Gamma})$	50	67	96	98	68	76	50
$\mathrm{Det}(\mathbf{\Gamma})$	37	47	98	99	60	68	37
$\|\mathbf{\Gamma}\|_F^2$	55	67	95	96	65	75	55
$1-H$	74	75	31	31	60	54	31
$\bar{\alpha}$	10	12	35	60	10	25	10
A	60	60	58	55	42	55	42
$\mathcal{P}_3$	78	78	37	37	64	59	37
$\mathcal{P}_H$	82	82	51	52	61	66	51
$\mathcal{P}_V$	71	64	35	35	61	53	35
$\mathcal{P}_{HV}$	64	63	23	22	36	42	22
$P_{db,fp}$	44	55	91	100	54	69	44
$P_{sb,fp}$	48	52	84	84	49	63	48
$P_{v,fp}$	12	21	86	96	26	48	12
$\langle|S_{HH}|^2\rangle$	54	63	91	95	55	71	54
$\langle2|S_{HV}|^2\rangle$	14	23	87	98	31	51	14
$\langle|S_{VV}|^2\rangle$	43	54	95	95	62	70	43
T_{22}	48	63	97	100	60	74	48
T_{11}	48	60	89	89	56	68	48
C_{RRRR}	37	46	93	99	52	65	37
C_{LLLL}	43	53	94	100	54	69	43
$\langle|S_8|^2\rangle$	41	53	88	91	53	65	41
$\langle|S_9|^2\rangle$	49	54	92	92	60	69	49
SDOP_1	70	75	31	29	50	51	29
SDOP_2	55	44	21	19	55	39	19
SDOP_3	11	12	10	12	10	11	10
SDOP_4	60	60	21	20	51	42	20
SDOP_5	66	69	52	70	33	58	33
SDOP_6	62	64	42	69	32	54	32
SDOP_7	60	60	55	66	42	57	42
SDOP_8	62	62	24	24	58	46	24
SDOP_9	61	61	26	26	53	45	26
$\langle k_h^2\rangle$	12	26	84	98	34	51	12
$P_{v,DF}$	14	23	87	98	31	51	14
$P_{db,DF}$	30	40	83	96	35	57	30
$P_{sb,DF}$	51	54	82	81	51	64	51
$P_{v,Yama}$	6	14	69	92	20	40	6
$P_{db,Yama}$	29	42	82	96	34	57	29
$P_{sb,Yama}$	50	57	88	88	52	67	50
$P_{h,Yama}$	25	36	86	96	40	56	25
$P_{db,VZ}$	43	53	96	100	48	68	43
$P_{sb,VZ}$	47	59	89	90	56	68	47
$P_{v,NNED}$	21	29	89	99	38	55	21
$P_{db,NNED}$	47	53	87	99	46	67	46
$P_{sb,NNED}$	51	56	85	83	52	65	51
$|\rho_{HHVV}|$	59	59	19	15	50	40	15
$1-|\rho_{HHVV}|$	0	0	1	5	0	1	0
$|C_{13}|$	51	56	87	86	55	67	51
$\mathcal{B}_\varphi$	1	2	17	61	0	16	0
$|\rho_{RRLL}|$	78	75	73	79	52	71	52
$|C_{RRLL}|$	58	64	95	100	56	75	56
δ_e	56	57	57	65	27	52	27
$|T_{13}|$	24	42	88	94	48	59	24
PMS	52	67	95	98	61	75	52

The values are the percentage of vehicles for which 5% of the vehicle's pixels, with a minimum of 10 pixels, have higher values than the 99.9th percentile of the corresponding natural cover type, for each considered polarimetric parameter.

over this type of cover. In particular, isolated deciduous trees, for example in fields, could be difficult to tell apart from vehicles due to similar size and shape. The span and Frobenius norm are behaving very similarly and are among the best parameters for the contrast they provide between vehicles and all natural cover types with the exception of deciduous trees. Instead, the best performing parameter to detect vehicles as opposed to deciduous trees is $|C_{RRLL}|$, which is giving excellent contrast as well between vehicles and the other natural cover types, with the exception of water meadows. The power received on the HH channel $\langle|S_{HH}|^2\rangle$ gives the same type of results as the latter. The double-bounce power obtained from some of the model-based decompositions (T_{22}, $P_{db,VZ}$, $P_{db,NNED}$) gives similar results, most likely because the signal cannot penetrate through the foliage at the *X*-band; hence, the double-bounce return on deciduous forests is low. The PMS stands out as offering some of the best contrast against all natural cover types, and has the best average and minimal value performance, making it the best individual polarimetric feature to use at the *X*-band.

At the *S*-band (see Table VI), the backscatter received from the coniferous and deciduous trees is quite similar, and the same parameters perform well to differentiate vehicles from these two cover types, namely $\mathcal{P}_3$ and $\mathcal{P}_H$. The backscatter emitted by trees is more depolarized than the one emitted by the vehicles, and this

TABLE VII
UNIVARIATE STUDY RESULTS FOR *L*-BAND DATA

Terrain type / Polarimetric parameter	Coniferous forest	Deciduous forest	Barren field	Grass field	Water-Meadow	Average	Minimal value
$Tr(\mathbf{\Gamma})$	31	41	65	91	50	56	31
$Det(\mathbf{\Gamma})$	17	32	83	100	53	57	17
$\|\|\mathbf{\Gamma}\|\|^2_F$	31	41	63	85	47	53	31
$1-H$	77	70	7	7	21	36	7
$\bar{\alpha}$	14	5	44	90	13	33	5
A	63	61	38	47	29	48	29
$\mathcal{P}_3$	86	78	7	7	30	42	7
$\mathcal{P}_H$	84	79	21	21	43	50	21
$\mathcal{P}_V$	76	73	6	5	27	37	5
$\mathcal{P}_{HV}$	51	55	5	5	19	27	5
$P_{db,fp}$	25	19	92	100	60	59	19
$P_{sb,fp}$	18	39	42	72	29	40	18
$P_{v,fp}$	0	3	67	100	24	39	0
$\langle|S_{HH}|^2\rangle$	30	43	70	95	52	58	30
$\langle 2|S_{HV}|^2\rangle$	0	3	68	100	35	41	0
$\langle|S_{VV}|^2\rangle$	22	30	57	78	44	46	22
T_{22}	32	21	93	100	61	61	21
T_{11}	22	42	45	75	34	44	22
C_{RRRR}	24	20	88	100	60	58	20
C_{LLLL}	21	23	90	100	60	59	21
$\langle|S_8|^2\rangle$	21	37	52	83	35	46	21
$\langle|S_9|^2\rangle$	20	38	50	78	32	44	20
$SDOP_1$	58	58	7	7	25	31	7
$SDOP_2$	52	46	4	4	11	24	4
$SDOP_3$	16	17	16	20	21	18	16
$SDOP_4$	58	60	5	5	13	28	5
$SDOP_5$	57	41	38	44	41	44	38
$SDOP_6$	53	37	36	49	36	42	36
$SDOP_7$	54	40	36	44	38	42	36
$SDOP_8$	58	63	4	5	14	29	4
$SDOP_9$	64	68	5	5	14	31	5
$\langle k_h^2\rangle$	2	12	83	100	40	48	2
$P_{v,DF}$	0	3	68	100	35	41	0
$P_{db,DF}$	17	15	86	99	53	54	15
$P_{sb,DF}$	21	45	45	71	28	42	21
$P_{v,Yama}$	0	0	48	98	23	34	0
$P_{db,Yama}$	17	15	85	98	54	53	15
$P_{sb,Yama}$	22	47	54	76	33	46	22
$P_{h,Yama}$	10	25	81	99	50	53	10
$P_{db,VZ}$	24	17	91	100	53	57	17
$P_{sb,VZ}$	20	42	48	78	31	44	20
$P_{v,NNED}$	1	10	67	100	35	43	1
$P_{db,NNED}$	25	18	86	99	47	55	18
$P_{sb,NNED}$	22	46	47	72	29	43	22
$|\rho_{HHVV}|$	49	54	4	5	14	25	4
$1-|\rho_{HHVV}|$	0	0	9	86	0	19	0
$|C_{13}|$	31	35	48	71	38	45	31
$\mathcal{B}_\varphi$	0	0	37	89	0	25	0
$|\rho_{RRLL}|$	74	50	43	62	30	52	30
$|C_{RRLL}|$	37	20	93	100	59	62	20
δ_e	32	33	32	73	18	38	18
$|T_{13}|$	6	18	56	97	30	41	6
PMS	31	42	72	95	59	60	31

The values are the percentage of vehicles for which 5% of the vehicle's pixels, with a minimum of 10 pixels, have higher values than the 99.9th percentile of the corresponding natural cover type, for each considered polarimetric parameter.

is slightly more visible in the horizontal polarization than in the vertical one, hence, the difference in results between $\mathcal{P}_H$ and $\mathcal{P}_V$. The correlation coefficient magnitude $|\rho_{RRLL}|$ is also a good choice to differentiate between forested covers and vehicles. The received power from the grass and barren field targets is low, therefore, making polarimetric parameters linked to the span relevant to detect vehicles. The best performing parameters are highlighted in the table. Finally, the span, Frobenius norm, and $\mathcal{P}_3$ are the best parameters to highlight vehicles as opposed to the water meadow. A structure appears in the results at the *S*-band, with different parameters giving good results on different types of natural covers, with no single parameter giving the best result over all natural cover types. In general, the degrees of polarization $\mathcal{P}_3, \mathcal{P}_H, \mathcal{P}_V$, seem to be able to highlight vehicles against areas with vegetation, as they tend to be low on areas with a high-volume scattering contribution. The total received power $Tr(\mathbf{\Gamma})$ and $\|\|\mathbf{\Gamma}\|\|^2_F$ work very well with different types of small crop fields or short grass areas, over which the total received intensity is low since the electromagnetic wave is reflected away from the radar antenna.

Finally, the results at the *L*-band (see Table VII) are similar to those obtained at *S*-band. $\mathcal{P}_3$ and $\mathcal{P}_H$ also give the best

results for the coniferous and deciduous forest covers. Volume scattering, unlike single-bounce or double-bounce scattering, is depolarizing; thus, the DoP is usually higher on vehicles than on forested areas. Five parameters stand out as they offer the best contrast between vehicles and the three remaining natural cover types, $P_{\mathrm{dp,fp}}$, T_{22}, C_{RRRR}, C_{LLLL}, and $|C_{\mathrm{RRLL}}|$. The first four parameters correspond to the power explained by double-bounce, dihedral scattering, and right-wound and left-wound helix scattering, respectively, thus bringing information both related to the total received power and the scattering mechanism. The last parameter $|C_{\mathrm{RRLL}}|$ is a bit more complex but also brings information related to the scattering mechanism and to the received power. These parameters manage to highlight vehicles well against the barren field, grass field, and water meadow cover due to the lower received intensities on these cover types than on the vehicles, and the scattering characterization, which is important for target detection at the L-band. The total received power is no longer part of the most interesting parameters to use on any natural cover, unlike at S- or X-bands. Furthermore, no individual parameter gives both the best average and minimal value over the five considered natural cover types; thus, no particular parameter stands out as the best choice for target detection using a single feature at the L-band. Three parameters, SDOP$_5$, SDOP$_6$, and SDOP$_7$, corresponding to the proximity with, respectively, dihedral scattering, left-wound helix, and right-wound helix scattering, give the best minimal performance for all natural covers simultaneously. This shows that at the L-band, characterizing the scattering mechanism is more important for target detection than the total received power. The double-bounce, right-, and left-wound helix scattering mechanisms are particularly important and relevant to analyze. A multivariate approach, making use of the different parameters highlighted here, should improve the detection capabilities at the L-band.

The structure of the results at S- and L-bands, for which different parameters with low correlation provide the best contrast between targets to detect and different groups of natural cover, is an indication that a multivariate approach, using these parameters together, would lead to better results. Furthermore, the total received power, often used for target detection in SAR images, appears to not always be the best parameter to use.

The parameters extracted from the $H-\alpha$ decomposition, seem to offer mediocre performance compared to some other features included in the univariate study. This univariate study highlights features that individually provide a stark contrast between the vehicles and natural covers and, therefore, might not be the best suited for natural cover classification and scene imaging. The strength of polarimetric decompositions and, in particular, the $H-\alpha$ decomposition is that their parameters have an excellent synergy and provide important information about polarimetric data when used together. Despite this, $1 - H$ behaves very similarly to the DoP $\mathcal{P}_3$ and was only slightly outperformed by it in S–L bands and comes very close to being highlighted in these tables. The average α angle does not provide a very good contrast between the vehicles and most natural covers, as it requires to be used together with the entropy to provide a good description of the scattering.

C. Summary

At the X-band, several polarimetric features stand out for target detection, namely $\mathrm{Tr}(\boldsymbol{\Gamma})$, $||\boldsymbol{\Gamma}||_F^2$, $\langle|S_{\mathrm{HH}}|^2\rangle$, C_{LLLL}, $|C_{\mathrm{RRLL}}|$, and PMS. All of those parameters are correlated with the received power, which is a central information for target detection in a natural cover at the X-band.

At S- and L- bands, the full DoP $\mathcal{P}_3$, the dual polarization DoP $\mathcal{P}_H$, and $|\rho_{\mathrm{RRLL}}|$ contain important information to tell apart vehicles from areas with vegetation, and high-volume scattering returns.

At S-band, $||\boldsymbol{\Gamma}||_F^2$, $\langle|S_{\mathrm{HH}}|^2\rangle$, $|\rho_{\mathrm{RRLL}}|$, $|C_{\mathrm{RRLL}}|$, and PMS give individually the best contrast between the vehicles and all the natural cover types under study.

At the L-band, the choice of polarimetric parameter to use should depend on the natural covers present in the scene, as a multivariate approach is needed to cover all situations. On nonwooded areas, $P_{\mathrm{db,fp}}$, C_{LLLL}, C_{RRRR}, and $|C_{\mathrm{RRLL}}|$ provide the best measured contrast.

V. MULTIVARIATE DETECTION

The use of several polarimetric parameters simultaneously enhances the detection capabilities, by making use of the relevant information kept in different features together. However, as presented earlier, there are many different informative parameters based on different approaches for target detection, often used separately. The goal of this study is to find subsets of features that used together maximize detection capabilities, for the three studied wavelengths, and do not require the computations of all the aforementioned parameters.

Target detection is akin to a binary classification where the two considered classes are target and natural cover. RF is well-known and established classifiers, already used in a number of polarimetric SAR applications such as [57], [58], [59]. They are a family of bootstrap aggregating (commonly called bagging) classifiers, training a specified number of classification trees on bootstrapped subsets of the data [60]. The classification decision performed by the RF is done by a majority voting of the individual trees. Each tree consists of a series of nodes that split the input data into two sets by thresholding on a feature in a way that minimizes the impurity of the two obtained sets. The impurity measure can be the entropy or the Gini criterion. The RF was trained on a pixel basis in the study, by aggregating all vehicle pixels for the target class and random subsets of the different natural covers to create the natural cover class. In this framework, pixels are classified individually, using their polarimetric parameters' values. Furthermore, the classifiers were trained on the polarimetric features after standardization to mean 0 and standard deviation 1. Whenever the data were split between train and test sets, the features' mean and standard deviation were estimated on the training data and applied to the test data.

A. Feature Reduction

The purpose of feature reduction is to select the optimal subsets of polarimetric parameters, which maximize the

classification performance, for a specified number of features. Several methodologies exist for feature reduction. The backward and forward selections are the two sides of the sequential feature selection. In the forward feature selection, the feature subset is built from the ground up by iteratively adding the feature that maximizes the model accuracy, whereas the backward selection iteratively removes the feature without which the model keeps the highest accuracy, such as in [61]. However, sequential feature selection is computationally prohibitive as it requires cross-validating and training the model a number of times equal to the number of features left in the model at every step. An alternative approach is the permutation feature importance, which rates each individual feature's importance by assessing the model accuracy decrease observed when its values are randomly shuffled. The decrease in model accuracy depends on the importance of said parameter for the model [60]. This measure is used in [57] for feature reduction for a multitemporal agricultural field classification. For RF classifiers, the Gini importance, called the impurity-based feature importance in the rest of this work to avoid confusion with the impurity criterion choice, is another way to rate features' importance. It is obtained as the sum of all impurities decreases obtained with the feature over all nodes of all trees in the RF [62]. For RF models using random subsets of parameters to train individual trees, this measure is normalized by the number of trees trained on a subset containing this feature.

Both permutation- and impurity-based feature importance measures are known to be biased for strongly correlated and multicollinear features. Strongly correlated features are removed by clustering features using Ward's linkage [63]. Ward's linkage is a hierarchical feature clustering algorithm, grouping clusters together to minimize within-cluster variance. The cluster distance $D = 0.3$ was used at all three wavelengths to form clusters, and one parameter was selected for each cluster. After this correlated feature removal, for all three wavelengths, an RF classifier was trained and used to rank the features both according to their permutation and impurity-based importance. The RF model used the entropy criterion, which yielded better results than the Gini criterion in a fivefold cross-validation, and 750 trees. The high number of trees in the model was necessary to ensure that the feature importance rankings were robust and reproducible.

The two rankings provided by the Gini and permutation importance assess how important a feature is to detect whether a pixel belongs to a vehicle or to a natural cover. The most important features, which appear first, are more crucial to the model than the others to make this classification. The results of this data-driven approach are a feature ranking, which can be used to create optimal feature subsets for distinguishing between vehicles and pixels natural cover pixels. The feature ranking obtained with the impurity-based importance is given in Table VIII, as it outperformed the ranking given by the permutation importance.

B. Accuracy Measures

Three metrics were used to evaluate the classification performance and the classifier's ability to distinguish between vehicle

TABLE VIII
IMPURITY-BASED FEATURE RANKING, FOR ALL THREE WAVELENGTHS, OBTAINED WITH RF CLASSIFIERS

	X-band	S-band	L-band
Feature 1	$P_{\text{db, fp}}$	$\lvert \rho_{\text{RRLL}} \rvert$	$\lvert \rho_{\text{RRLL}} \rvert$
Feature 2	$\text{Tr}(\mathbf{\Gamma})$	$P_{v,\text{Yama}}$	SDOP_5
Feature 3	$P_{\text{db, Yama}}$	$P_{h,\text{Yama}}$	$\text{Det}(\mathbf{\Gamma})$
Feature 4	$\lvert \rho_{\text{RRLL}} \rvert$	A	A
Feature 5	$P_{h,\text{Yama}}$	SDOP_5	$\text{Tr}(\mathbf{\Gamma})$
Feature 6	$P_{\text{sb, Yama}}$	$\mathcal{P}_V$	SDOP_7
Feature 7	$P_{v,\text{fp}}$	$P_{\text{db, fp}}$	$P_{h,\text{Yama}}$
Feature 8	$\mathcal{P}_V$	δ_e	$P_{v,\text{Yama}}$
Feature 9	SDOP_5	$P_{\text{db, Yama}}$	$P_{v,\text{fp}}$

and natural pixels. The first measured is the overall accuracy, ranging from 0 to 1, and represents the ratio of correct classifications. The second metric is Cohen's Kappa score, which is a measure of categorical agreement on a classification, and takes into account the probability that the agreement is due to chance

$$\kappa = \frac{p_0 - p_e}{1 - p_e} \tag{28}$$

where p_0 is the ratio of classifications on which the two annotators agree and p_e is expected agreement when both classifications are random [64]. The score ranges from 1 for perfect agreement to -1 for complete chance agreement. This makes the κ score a measure close yet more robust than the overall accuracy. The third and last metric used is the F1 score defined as

$$F1 = 2 \times \frac{\text{precision} \times \text{recall}}{\text{precision} + \text{recall}}. \tag{29}$$

The precision and recall are defined, respectively, as

$$\text{precision} = \frac{\text{true positives}}{\text{true positives} + \text{false positives}}$$

$$\text{recall} = \frac{\text{true positives}}{\text{true positives} + \text{false negatives}} \tag{30}$$

where a vehicle pixel is considered a positive and a natural cover pixel a negative. The F1 score is the harmonic mean between precision and recall and ranges from 0 to 1. In this setting, the recall is, therefore, the probability of detection on a pixel basis while the precision corresponds to the ratio of correct detections over all detections.

C. Optimal Feature Subsets and Classification Accuracy Improvements

The optimal subsets containing k features are created using the first k features from either the permutation or impurity-based feature importance rankings. The classification accuracy using RF classifiers on subsets containing $k \in [1, 9]$ features is measured using the three scores presented previously, using the same methodology for all wavelengths. The dataset is randomly split $3/4{:}1/4$ into a train and test set. RF classifiers with 100 trees with the entropy criterion are trained on the same train set using the first $k \in [1, 9]$ features from both the permutation and impurity-based rankings. The classification accuracy achieved is then evaluated on the test set and the obtained accuracy scores as a function of the number of features in the subset
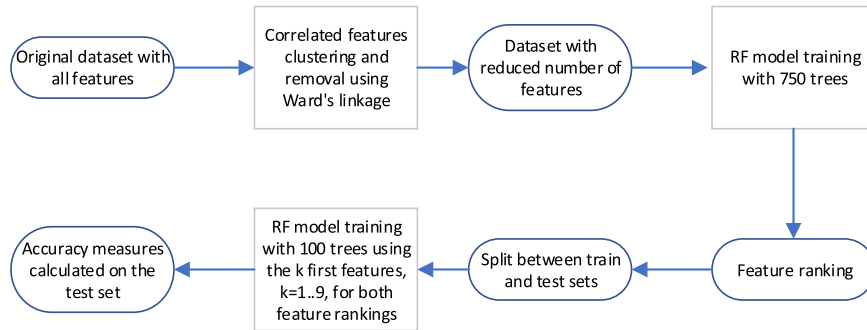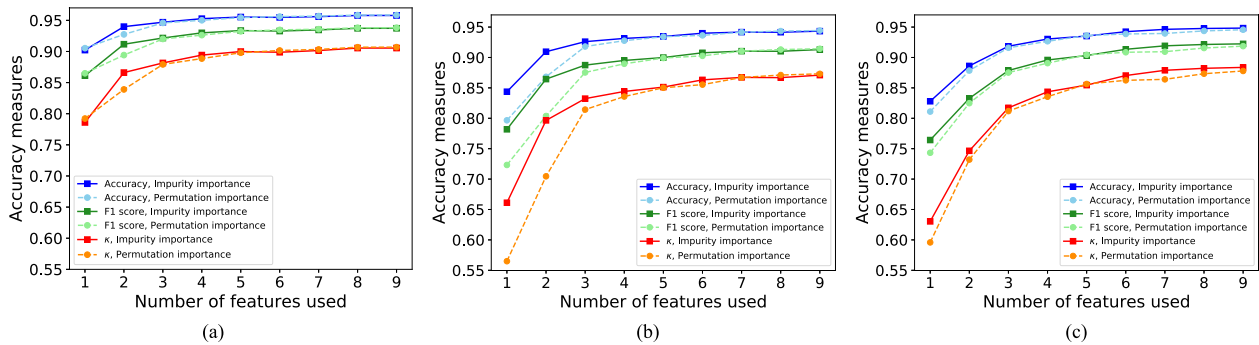
Fig. 4. Flowchart summarizing the data processing.

Fig. 5. Accuracy scores obtained on test data for RF models using the $k \in [1, 9]$ most important features according to the permutation and impurity-based feature importance. (a) X-band. (b) S-band. (c) L-band.

are plotted in Fig. 5. The feature ranking provided by the impurity-based importance outperforms the one given by the permutation importance for models using few features; hence, only the impurity-based importance ranking is provided. The graph scales are the same for all subimages in Fig. 5, for a straightforward comparison of the classification and detection capabilities with the different wavelengths. The nine first-ranked features according to the impurity-based importance for all three wavelengths are reported in Table VIII. Finally, a flowchart in Fig. 4 summarizes the methodology applied at each wavelength to obtain the feature rankings and accuracy scores for increasing the size of feature subsets.

The classification accuracy at the X-band is high, even when the feature subset contains only a few parameters. The overall accuracy classification accuracy is 90% with only one feature and improves to 94% with the addition of the second feature. The addition of a second feature brings a clear improvement to the classification accuracy, with a F1 score improving from 0.86 to 0.91, and the κ score going from 0.79 to 0.87. The addition of other features to the subset brings marginal improvements to the model, until the fifth feature.

In contrast, the classification accuracy for S- and L-bands when using only one feature is much lower, as expected from the univariate study results. For a subset containing two features, the overall classification accuracy at the S-band is 91% and is slightly below 89% at the L-band. However, the classification accuracy benefits more from the introduction of additional features in the subset. At the S-band, the

classification accuracy improves rapidly until the subset contains three features and continues to improve slowly until the subset contains six features, at which point the overall accuracy is 94%, with an F1 score of 0.91 and a κ score of 0.86. At the L-band, the classification accuracy progresses rapidly with the introduction of additional features until the subset contains four features, and smaller improvements are visible until seven features are used together. With seven features at the L-band, the classification's overall accuracy is 94.5%, the F1 score is 0.92, and the κ score is 0.88.

The classification accuracy increase at S- and L-bands with the addition of features is such that it is comparable, though still slightly lower, to what can be achieved in the X-band. This supports the observation that a multivariate approach is more important as the wavelength increases since the relevant information for target detection is more distributed between several polarimetric features than at the X-band. It is also worth noticing that less features are required at the S-band than at the L-band to obtain the same classification accuracy.

D. Feature Subsets Analysis

The features and their ordering given in Table VIII correspond to the feature subsets of which the accuracies are plotted as solid lines in Fig. 5. Furthermore, the most correlated features were clustered together with Ward's linkage before determining the feature importance ranking with the impurity-based importance, and one feature was kept per cluster. Features from the same

TABLE IX
POLARIMETRIC FEATURES BELONGING TO THE SAME CLUSTERS AS THE HIGHEST RANKED FEATURES USING THE IMPURITY-BASED FEATURE RANKING

Features (denoted earlier) / Wavelength	X-band	S-band	L-band
$P_{\mathrm{db,fp}}$	$T_{22}, P_{\mathrm{db,VZ}}, C_{\mathrm{RRRR}}, C_{\mathrm{LLLL}}, \|C_{\mathrm{RRLL}}\|$	$T_{22}, P_{\mathrm{db,VZ}}, C_{\mathrm{RRRR}}, C_{\mathrm{LLLL}}, \|C_{\mathrm{RRLL}}\|$	x
$\mathrm{Tr}(\boldsymbol{\Gamma})$	$\|\|\boldsymbol{\Gamma}\|\|_F^2, PMS, \mathrm{Det}(\boldsymbol{\Gamma}), \langle\|S_{\mathrm{HH}}\|^2\rangle, \langle\|S_8\|^2\rangle, \langle\|S_9\|^2\rangle, T_{11}, \langle\|S_{\mathrm{VV}}\|^2\rangle$	x	$\|\|\boldsymbol{\Gamma}\|\|_F^2, PMS, \langle\|S_{\mathrm{HH}}\|^2\rangle, \langle\|S_8\|^2\rangle, \langle\|S_9\|^2\rangle, T_{11}, \langle\|S_{\mathrm{VV}}\|^2\rangle$
$P_{\mathrm{db,Yama}}$	$P_{\mathrm{db,DF}}, P_{\mathrm{db,NNED}}$	$P_{\mathrm{db,DF}}, P_{\mathrm{db,NNED}}$	x
$\|\rho_{\mathrm{RRLL}}\|$	/	/	/
$P_{h,\mathrm{Yama}}$	/	/	/
$P_{\mathrm{sb,Yama}}$	$P_{\mathrm{sb,DF}}, P_{\mathrm{sb,NNED}}$	x	x
$P_{v,\mathrm{fp}}$	$\langle k_h^2\rangle, P_{v,\mathrm{NNED}}, P_{v,\mathrm{VZ}}, \langle\|S_{\mathrm{HV}}\|^2\rangle, P_{v,\mathrm{DF}}$	x	$\langle k_h^2\rangle, P_{v,\mathrm{NNED}}, P_{v,\mathrm{VZ}}, \langle\|S_{\mathrm{HV}}\|^2\rangle, P_{v,\mathrm{DF}}$
$\mathcal{P}_V$	/	/	x
SDOP_5	SDOP_6	SDOP_6	SDOP_6
$P_{v,\mathrm{Yama}}$	x	/	/
A	x	/	/
δ_e	x	/	x
$\mathrm{Det}(\boldsymbol{\Gamma})$	x	x	$C_{\mathrm{RRRR}}, C_{\mathrm{LLLL}}, \|C_{\mathrm{RRLL}}\|, P_{\mathrm{db,VZ}}, T_{22}, P_{\mathrm{db,fp}},$
SDOP_7	x	x	/

Cases with "/" means that no other features are in the cluster, and cases with "x" stand for features not selected as one of the most important ones at the specific wavelength.

cluster are highly correlated and contain similar information. Several features from Table VIII belong to such clusters and can, therefore, be replaced by other features from their respective clusters, which are listed in Table IX. The feature ordering in this table follows a top-to-bottom reading order from Table VIII. A "/" sign in the table indicates that the feature is clustered alone and cannot be replaced, and an "x" sign indicates that the feature is not listed for this wavelength as one of the most important features in Table VIII. In the same way as for the univariate study, the description of results refers to the different bands individually. The influence of the different spatial resolutions between the bands on these results is not assessed here but is important to keep in mind.

At the X-band, the first two features, which are the most important features, are $P_{\mathrm{db,fp}}$ and the total received power $\mathrm{Tr}(\boldsymbol{\Gamma})$. Among others, $P_{\mathrm{db,fp}}$ is clustered with T_{22} and $\|C_{\mathrm{RRLL}}\|$, which might also be used as an alternative in the model. These two components did appear complementary in the univariate study, in which the total received power managed to highlight well vehicles against all types of natural covers with the exception of deciduous forest while $P_{\mathrm{db,fp}}$ and variables correlated with it managed to highlight vehicles well against this type of cover while also giving one of the best average and minimal-value contrast on all the selected natural covers. The span is also clustered together with the PMS, which was the best performing individual parameter overall at the X-band. The following three features bring small classification accuracy improvements, which means that their specific ordering is less important.

At the S-band, the three most important features are $\|\rho_{\mathrm{RRLL}}\|$, and the power explained by volume scattering $P_{v,\mathrm{Yama}}$ and helix scattering $P_{h,\mathrm{Yama}}$ in the decomposition proposed by Yamaguchi. None of these three features are clustered with any other feature, which means that they cannot be replaced with another feature and makes the information they bring particularly valuable. It is interesting to point out that at the S-band, $\|\rho_{\mathrm{RRLL}}\|$ was part of the best individual features to use for vehicle detection, for its generalization capacity against all the selected natural

cover types. The three next most important features at the S-band, which bring additional classification improvements are the anisotropy A, the closeness to dihedral scattering SDOP_5, and the DoP $\mathcal{P}_V$. Out of these features, only SDOP_5 is close and clustered together with another feature, which is the closeness with left-wound helix scattering SDOP_6. Interestingly, the total received power, and the most correlated features with it like the PMS and the Frobenius norm $\|\|\boldsymbol{\Gamma}\|\|_F^2$ are not part of the optimal feature subsets at the S-band, despite being highlighted as some of the best individual features in the univariate study. It means that the received power information is already brought in the subset by the powers from the Yamaguchi decomposition, which are the only features somewhat correlated with the span.

Finally, at the L-band, the model accuracy improves quickly until the subset contains four features, which makes their ordering particularly important. The subset's most important feature is $\|\rho_{\mathrm{RRLL}}\|$, just like at the S-band, and is not clustered with any other polarimetric parameter. The second feature in the subset is SDOP_5, which represents how close the scattering is to dihedral scattering. This parameter is clustered together with SDOP_6, which is the closeness of the scattering with a pure left-wound helix scattering. The third most important feature is the determinant $\mathrm{Det}(\boldsymbol{\Gamma})$, which is not clustered together with the total received power, but with the group described in Table IX containing among others some double-bounce powers like T_{22} and $\|C_{\mathrm{RRLL}}\|$. The fourth most important feature is, just like at the S-band, the anisotropy A, which is not clustered with any other feature. This list shows that at the L-band, the nature of the scattering itself is more important to detect vehicles than only relying upon the total received power. The next three features, which bring small classification improvements are the total received power $\mathrm{Tr}(\boldsymbol{\Gamma})$, the scattering closeness to the right-wound helix SDOP_7, and the helix power from the Yamaguchi decomposition. Helix scattering plays a major role in target detection at the L-band, as can be seen with the importance of $\|\rho_{\mathrm{RRLL}}\|$, the determinant that is closely linked to $\|C_{\mathrm{RRLL}}\|$, the presence of the SDOP features for both helix

directions, and the helix power from the decomposition proposed by Yamaguchi.

Interestingly, the DoPs $\mathcal{P}_3$ and $\mathcal{P}_H$, highlighted in the univariate study as being able to differentiate between forested areas and vehicles very well at *S*- and *L*-bands, were not part of the optimal feature subsets derived. Instead, the subsets contain the feature $|\rho_{\text{RRLL}}|$, which was also able to highlight vehicles against forested areas well, and generalized better to other natural cover types. The information brought by this feature is particularly valuable for target detection, as it appears in the subsets of interest for all wavelengths, and cannot be replaced by another polarimetric parameter, as it is alone in its cluster group. Similarly, the power explained by helix scattering $P_{h,\text{Yama}}$ also belongs to the polarimetric subsets at all wavelengths and cannot be replaced either by a closely related parameter. This is also true for the anisotropy A, which is an important parameter at *S*- and *L*-bands, and is not highly correlated with any other feature, which also makes it particularly valuable.

The total received power while particularly important for target detection at the *X*-band becomes less relevant at *S*- and *L*-bands, for which the nature of the scattering brings more information for target detection. It is, however, still part of the subsets either directly at *X*- and *L*-bands, or indirectly at the *S*-band through the two power parameters from the decomposition proposed by Yamaguchi. A shift happens in the information brought by the determinant $\text{Det}(\boldsymbol{\Gamma})$ as the wavelength increases. It is first highly correlated to the span at *X*- and *S*-bands and belongs to the same cluster group. At the *L*-band, the determinant is instead clustered with some double-bounce powers ($P_{\text{db,fp}}$, T_{22}, $P_{\text{db,VZ}}$), as well as C_{RRRR}, C_{LLLL}, and $|C_{\text{RRLL}}|$.

E. Summary

The multivariate study confirmed that 1) for all considered wavelengths, the use of several complementary polarimetric features improved the detection accuracy, and 2) that the improvement observed was more important for the *L*-band than for the *S*-band, and likewise more important for the *S*-band than the *X*-band. The optimal subsets found are shown in Table VIII. Once again, at the *X*-band, the most important parameters are linked to the total received power and double-bounce scattering. At *S*- and *L*-bands, the parameters characterizing the helicity and the nature of the scattering mechanism were very important for target detection.

VI. Conclusion

We presented a review of polarimetric decompositions and features regularly used in polarimetric SAR applications, with a strong emphasis on multilooked features for speckle reduction. All the polarimetric features are evaluated after orientation angle correction on the covariance matrices, and the different features presented are linked to the physical properties of scatterers. A large high-resolution dataset, containing in total 297 individual vehicles with different orientations compared to the radar line of sight, seen under different depression angles, and acquired in *X*-, *S*-, and *L*-bands is used as a basis to evaluate the features' capabilities for vehicle detection. The results presented can be

used to improve vehicle detection in nonurban areas, by selecting the most relevant polarimetric features subsets. However, one must be aware that this study focused only on a few types of natural covers and that polarimetric scattering can change with different atmospheric effects (after rainy days, or under windy conditions for example). Furthermore, the spatial resolution of the radar can also influence some of these results, which means that all the differences observed between the wavelengths cannot only be explained by the wavelength difference.

The first objective of the study was to provide a quantitative assessment of the detection capabilities of the individual features, over the three wavelengths. The goal of this approach was to find the features with high values on the vehicles compared to different types of natural clutter and can be used to distinguish one from the other. Another key observation was that using a single feature, the best average detection capabilities have a downward tendency from *X*- to *L*-bands. At *S*- and *L*-bands, a structure is visible in the table of results, where different features give the best contrast between the vehicles and different natural cover types. The span, often used for target detection in univariate approaches, is not always the only or the best parameter to use for target detection against natural covers.

The study's second objective was to find subsets of polarimetric features, which used together give the best detection performance. The optimal subsets for target detection were determined and given for each wavelength using RF classifiers and using the impurity-based feature ranking, which is a data-driven approach. This study confirmed that a multivariate approach is more and more important as the wavelength increases. Comparable detection performance can be obtained at all wavelengths, using more features in the subset from *X*- to *L*-bands. Nevertheless, the multivariate approach improved detection results, even at the *X*-band, for which a large improvement was found by using two features together.

Future work on this topic could include a comparative study for target detection using the subsets obtained in this study and more traditional approaches, in which the feature subset is obtained using the parameters from a polarimetric decomposition. An alternative approach to single-look complex data focusing on the coherent decompositions presented could also be considered.

References

[1] K. El-Darymli, P. McGuire, D. Power, and C. R. Moloney, "Target detection in synthetic aperture radar imagery: A state-of-the-art survey," *J. Appl. Remote Sens.*, vol. 7, no. 1, 2013, Art. no. 071598.

[2] L. M. Novak, G. J. Owirka, and C. M. Netishen, "Performance of a high-resolution polarimetric SAR automatic target recognition system," *Lincoln Lab. J.*, vol. 6, no. 1, pp. 11–24, 1993.

[3] M. di Bisceglie and C. Galdi, "CFAR detection of extended objects in high-resolution SAR images," *IEEE Trans. Geosci. Remote Sens.*, vol. 43, no. 4, pp. 833–843, Apr. 2005.

[4] G. Gao, L. Liu, L. Zhao, G. Shi, and G. Kuang, "An adaptive and fast CFAR algorithm based on automatic censoring for target detection in high-resolution SAR images," *IEEE Trans. Geosci. Remote Sens.*, vol. 47, no. 6, pp. 1685–1697, Jun. 2009.

[5] H. Dai, L. Du, Y. Wang, and Z. Wang, "A modified CFAR algorithm based on object proposals for ship target detection in SAR images," *IEEE Geosci. Remote Sens. Lett.*, vol. 13, no. 12, pp. 1925–1929, Dec. 2016.

[6] N. Wang, G. Shi, L. Liu, L. Zhao, and G. Kuang, "Polarimetric SAR target detection using the reflection symmetry," *IEEE Geosci. Remote Sens. Lett.*, vol. 9, no. 6, pp. 1104–1108, Nov. 2012.

[7] G. Gao, "A Parzen-window-kernel-based CFAR algorithm for ship detection in SAR images," *IEEE Geosci. Remote Sens. Lett.*, vol. 8, no. 3, pp. 557–561, May 2011.

[8] J. Chen, Y. Chen, and J. Yang, "Ship detection using polarization cross-entropy," *IEEE Geosci. Remote Sens. Lett.*, vol. 6, no. 4, pp. 723–727, Oct. 2009.

[9] L. Novak, "Target detection studies using fully polarimetric data collected by the Lincoln laboratory MMW SAR," in *Proc. Int. Conf. Radar*, 1992, pp. 167–170.

[10] A. Marino, S. R. Cloude, and I. H. Woodhouse, "A polarimetric target detector using the Huynen fork," *IEEE Trans. Geosci. Remote Sens.*, vol. 48, no. 5, pp. 2357–2366, May 2010.

[11] A. Marino, N. Walker, and I. Woodhouse, "Ship detection with RADARSAT-2 quad-pol SAR data using a notch filter based on perturbation analysis," in *Proc. IEEE Int. Geosci. Remote Sens. Symp.*, 2010, pp. 3704–3707.

[12] G. D. De Grandi, J.-S. Lee, and D. L. Schuler, "Target detection and texture segmentation in polarimetric SAR images using a wavelet frame: Theoretical aspects," *IEEE Trans. Geosci. Remote Sens.*, vol. 45, no. 11, pp. 3437–3453, Nov. 2007.

[13] A. Mian, J.-P. Ovarlez, A. M. Atto, and G. Ginolhac, "Design of new wavelet packets adapted to high-resolution SAR images with an application to target detection," *IEEE Trans. Geosci. Remote Sens.*, vol. 57, no. 6, pp. 3919–3932, Jun. 2019.

[14] Z. Cao, Y. Ge, and J. Feng, "Fast target detection method for high-resolution SAR images based on variance weighted information entropy," *EURASIP J. Adv. Signal Process.*, vol. 2014, no. 1, pp. 1–11, 2014.

[15] T. Li, Z. Liu, L. Ran, and R. Xie, "Target detection by exploiting superpixel-level statistical dissimilarity for SAR imagery," *IEEE Geosci. Remote Sens. Lett.*, vol. 15, no. 4, pp. 562–566, Apr. 2018.

[16] W. Yu, Y. Wang, H. Liu, and J. He, "Superpixel-based CFAR target detection for high-resolution SAR images," *IEEE Geosci. Remote Sens. Lett.*, vol. 13, no. 5, pp. 730–734, May 2016.

[17] Z. Wang, L. Du, J. Mao, B. Liu, and D. Yang, "SAR target detection based on SSD with data augmentation and transfer learning," *IEEE Geosci. Remote Sens. Lett.*, vol. 16, no. 1, pp. 150–154, Jan. 2019.

[18] L. Du, L. Li, D. Wei, and J. Mao, "Saliency-guided single shot multibox detector for target detection in SAR images," *IEEE Trans. Geosci. Remote Sens.*, vol. 58, no. 5, pp. 3366–3376, May 2020.

[19] S. R. Cloude and E. Pottier, "A review of target decomposition theorems in radar polarimetry," *IEEE Trans. Geosci. Remote Sens.*, vol. 34, no. 2, pp. 498–518, Mar. 1996.

[20] R. Touzi, "Polarimetric target scattering decomposition: A review," in *Proc. IEEE Int. Geosci. Remote Sens. Symp.*, 2016, pp. 5658–5661.

[21] R. Touzi, "Target scattering decomposition in terms of roll-invariant target parameters," *IEEE Trans. Geosci. Remote Sens.*, vol. 45, no. 1, pp. 73–84, Jan. 2007.

[22] A. Freeman and S. L. Durden, "A three-component scattering model for polarimetric SAR data," *IEEE Trans. Geosci. Remote Sens.*, vol. 36, no. 3, pp. 963–973, May 1998.

[23] Y. Yamaguchi, T. Moriyama, M. Ishido, and H. Yamada, "Four-component scattering model for polarimetric SAR image decomposition," *IEEE Trans. Geosci. Remote Sens.*, vol. 43, no. 8, pp. 1699–1706, Aug. 2005.

[24] E. Krogager, "New decomposition of the radar target scattering matrix," *Electron. Lett.*, vol. 26, no. 18, pp. 1525–1527, 1990.

[25] J.-S. Lee, D. L. Schuler, T. L. Ainsworth, E. Krogager, D. Kasilingam, and W.-M. Boerner, "On the estimation of radar polarization orientation shifts induced by terrain slopes," *IEEE Trans. Geosci. Remote Sens.*, vol. 40, no. 1, pp. 30–41, Jan. 2002.

[26] Y. Yamaguchi, A. Sato, W.-M. Boerner, R. Sato, and H. Yamada, "Four-component scattering power decomposition with rotation of coherency matrix," *IEEE Trans. Geosci. Remote Sens.*, vol. 49, no. 6, pp. 2251–2258, Jun. 2011.

[27] J.-S. Lee and T. L. Ainsworth, "The effect of orientation angle compensation on coherency matrix and polarimetric target decompositions," *IEEE Trans. Geosci. Remote Sens.*, vol. 49, no. 1, pp. 53–64, Jan. 2011.

[28] J. Praks, E. C. Koeniguer, and M. T. Hallikainen, "Alternatives to target entropy and alpha angle in SAR polarimetry," *IEEE Trans. Geosci. Remote Sens.*, vol. 47, no. 7, pp. 2262–2274, Jul. 2009.

[29] A. C. Frery, H.-J. Muller, C. d. C. F. Yanasse, and S. J. S. Sant' Anna, "A model for extremely heterogeneous clutter," *IEEE Trans. Geosci. Remote Sens.*, vol. 35, no. 3, pp. 648–659, May 1997.

[30] C. C. Freitas, A. C. Frery, and A. H. Correia, "The polarimetric G distribution for SAR data analysis," *Environmetrics: Official J. Int. Environmetrics Soc.*, vol. 16, no. 1, pp. 13–31, 2005.

[31] R. Shirvany, "Estimation of the degree of polarization in polarimetric SAR imagery: Principles and applications," Ph.D. dissertation, Institut de Recherche en Informatique de Toulouse, INP Toulouse, Toulouse, France, 2012.

[32] S. Dey, A. Bhattacharya, D. Ratha, D. Mandal, and A. C. Frery, "Target characterization and scattering power decomposition for full and compact polarimetric SAR data," *IEEE Trans. Geosci. Remote Sens.*, vol. 59, no. 5, pp. 3981–3998, May 2021.

[33] R. Barakat, "Degree of polarization and the principal idempotents of the coherency matrix," *Opt. Commun.*, vol. 23, no. 2, pp. 147–150, 1977.

[34] J. R. Huynen, "Phenomenological theory of radar targets," Ph.D. dissertation, Elect. Eng., Math. Comput. Sci., Tech. Univ., Delft, The Netherlands, 1970.

[35] D. Li and Y. Zhang, "Unified Huynen phenomenological decomposition of radar targets and its classification applications," *IEEE Trans. Geosci. Remote Sens.*, vol. 54, no. 2, pp. 723–743, Feb. 2016.

[36] V. Alberga, G. Satalino, and D. Staykova, "Comparison of polarimetric SAR observables in terms of classification performance," *Int. J. Remote Sens.*, vol. 29, no. 14, pp. 4129–4150, 2008.

[37] E. Krogager, W.-M. Boerner, and S. N. Madsen, "Feature-motivated Sinclair matrix (sphere/diplane/helix) decomposition and its application to target sorting for land feature classification," *Proc. SPIE*, vol. 3120, pp. 144–154, 1997.

[38] J. J. van Zyl, "Application of Cloude's target decomposition theorem to polarimetric imaging radar data," *Proc. SPIE*, vol. 1748, pp. 184–191, 1993.

[39] J. J. Van Zyl, M. Arii, and Y. Kim, "Model-based decomposition of polarimetric SAR covariance matrices constrained for nonnegative eigenvalues," *IEEE Trans. Geosci. Remote Sens.*, vol. 49, no. 9, pp. 3452–3459, Sep. 2011.

[40] S. Nghiem, S. Yueh, R. Kwok, and D. Nguyen, "Polarimetric remote sensing of geophysical medium structures," *Radio Sci.*, vol. 28, no. 6, pp. 1111–1130, 1993.

[41] B. B. Thomsen, S. Nghiem, and R. Kwok, "Polarimetric C-band SAR observations of sea ice in the Greenland Sea," in *Proc. 98th Sens. Manage. Environ. IEEE Int. Geosci. Remote Sens. Symp. Proc.*, 1998, pp. 2502–2504.

[42] S. Nghiem, S. Yueh, R. Kwok, and F. Li, "Symmetry properties in polarimetric remote sensing," *Radio Sci.*, vol. 27, no. 5, pp. 693–711, 1992.

[43] F. Nunziata, M. Migliaccio, and C. E. Brown, "Reflection symmetry for polarimetric observation of man-made metallic targets at sea," *IEEE J. Ocean. Eng.*, vol. 37, no. 3, pp. 384–394, Jul. 2012.

[44] F. Nunziata and M. Migliaccio, "On the COSMO-Skymed pingpong mode to observe metallic targets at sea," *IEEE J. Ocean. Eng.*, vol. 38, no. 1, pp. 71–79, Jan. 2012.

[45] M. Migliaccio, F. Nunziata, and A. Gambardella, "On the co-polarized phase difference for oil spill observation," *Int. J. Remote Sens.*, vol. 30, no. 6, pp. 1587–1602, 2009.

[46] M. Migliaccio, F. Nunziata, and A. Buono, "SAR polarimetry for effective sea oil slick observation," in *Proc. IEEE/OES Baltic Int. Symp.*, 2018, pp. 1–5.

[47] F. Nunziata, A. Gambardella, and M. Migliaccio, "A unitary Mueller-based view of polarimetric SAR oil slick observation," *Int. J. Remote Sens.*, vol. 33, no. 20, pp. 6403–6425, 2012.

[48] F. Ulaby, K. Sarabandi, and A. Nashashibi, "Statistical properties of the Mueller matrix of distributed targets," *Proc. Inst. Elect. Eng.—F Radar Signal Process.*, vol. 139, no. 2, pp. 136–146, 1992.

[49] Y. Yamaguchi, *Polarimetric SAR Imaging: Theory and Applications*. Boca Raton, FL, USA: CRC Press, 2020.

[50] T. Ishikuro, R. Sato, Y. Yamaguchi, and H. Yamada, "A fundamental study on vehicle detection in flooded urban area using quad-polarimetric SAR data," *IEICE Trans. Electron.*, vol. 102, no. 1, pp. 38–45, 2019.

[51] T. Ainsworth, D. Schuler, and J.-S. Lee, "Polarimetric SAR characterization of man-made structures in urban areas using normalized circular-pol correlation coefficients," *Remote Sens. Environ.*, vol. 112, no. 6, pp. 2876–2885, 2008.

[52] K. Kimura, Y. Yamaguchi, T. Moriyama, and H. Yamada, "Circular polarization correlation coefficient for detection of non-natural targets aligned not parallel to SAR flight path in the X-band POLSAR image analysis," *IEICE Trans. Commun.*, vol. 87, no. 10, pp. 3050–3056, 2004.

[53] W.-M. Boerner, A. Kostinski, and B. James, "On the concept of the polarimetric matched filter in high resolution radar imaging: An alternative for speckle radiation," *Remote Sens.: Moving Towards 21st Century*, vol. 1, pp. 69–72, 1988.

[54] R. Chaney, M. Bud, and L. Novak, "On the performance of polarimetric target detection algorithms," *IEEE Aerosp. Electron. Syst. Mag.*, vol. 5, no. 11, pp. 10–15, Nov. 1990.

[55] S. Allain, L. Ferro-Famil, E. Pottier, and J. Fortuny, "Influence of resolution cell size for surface parameters retrieval from polarimetric SAR data," in *Proc. IEEE Int. Geosci. Remote Sens. Symp.*, 2003, pp. 440–442.

[56] K. Zhang, X. Xu, B. Han, L. R. Mansaray, Q. Guo, and J. Huang, "The influence of different spatial resolutions on the retrieval accuracy of sea surface wind speed with C-2PO models using full polarization C-band SAR," *IEEE Trans. Geosci. Remote Sens.*, vol. 55, no. 9, pp. 5015–5025, Sep. 2017.

[57] L. Loosvelt, J. Peters, H. Skriver, B. De Baets, and N. E. Verhoest, "Impact of reducing polarimetric SAR input on the uncertainty of crop classifications based on the random forests algorithm," *IEEE Trans. Geosci. Remote Sens.*, vol. 50, no. 10, pp. 4185–4200, Oct. 2012.

[58] Y. Yu, M. Li, and Y. Fu, "Forest type identification by random forest classification combined with SPOT and multitemporal SAR data," *J. Forestry Res.*, vol. 29, no. 5, pp. 1407–1414, 2018.

[59] M. Mahdianpari, B. Salehi, F. Mohammadimanesh, and B. Brisco, "An assessment of simulated compact polarimetric SAR data for wetland classification using random forest algorithm," *Can. J. Remote Sens.*, vol. 43, no. 5, pp. 468–484, 2017.

[60] L. Breiman, "Random forests," *Mach. Learn.*, vol. 45, no. 1, pp. 5–32, 2001.

[61] S. F. Abdoh, M. A. Rizka, and F. A. Maghraby, "Cervical cancer diagnosis using random forest classifier with SMOTE and feature reduction techniques," *IEEE Access*, vol. 6, pp. 59475–59485, 2018.

[62] S. Nembrini, I. R. König, and M. N. Wright, "The revival of the Gini importance?," *Bioinformatics*, vol. 34, no. 21, pp. 3711–3718, 2018.

[63] J. H. Ward, Jr., and M. E. Hook, "Application of an hierarchical grouping procedure to a problem of grouping profiles," *Educ. Psychol. Meas.*, vol. 23, no. 1, pp. 69–81, 1963.

[64] J. Cohen, "A coefficient of agreement for nominal scales," *Educ. Psychol. Meas.*, vol. 20, no. 1, pp. 37–46, 1960.

Paul Connetable received the M.Sc. degree in general engineering from Ecole Centrale Nantes, Nantes, France, and the second M.Sc. and Ph.D. degrees in earth observation from the Technical University of Denmark (DTU), Kongens Lyngby, Denmark, in 2017 and 2022, respectively.

His main research interests include the application of statistics to polarimetric SAR images, and the detection and classification of man-made structures in polarimetric SAR images.
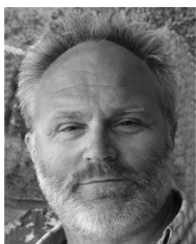
Allan Aasbjerg Nielsen received the M.Sc. degree in electrophysics and Ph.D. degree in mathematical modelling from the Technical University of Denmark (DTU), Kongens Lyngby, Denmark, in 1978 and 1994, respectively.

From 1977 to 1978, he was with Danish Defense Research Establishment. From 1978 to 1985, he worked on energy conservation in housing with the Thermal Insulation Laboratory, DTU. He was with the section for image analysis from 1985 to 2001 and with the section for geoinformatics from 2001 to 2006, both at the Department of Informatics and Mathematical Modeling, DTU. From 2007 to 2013, he was with Danish National Space Center's section for geodesy. From 2013 to 2020, he was an Associate Professor with the Department of Applied Mathematics and Computer Science, DTU, where he is currently Emeritus. Since 1985, he has been working on several national and international projects on the development, implementation, and application of statistical methods, and remote sensing in mineral exploration, mapping, geology, agriculture, environmental monitoring, oceanography, geodesy, and security funded by industry, the European Union, the Danish International Development Agency (Danida), and the Danish National Research Councils.

Knut Conradsen received the Candidatus Scientiarum degree in mathematics from the University of Copenhagen, Copenhagen, Denmark, in 1970.

Since 1970, he has been with the Technical University of Denmark (DTU), Kongens Lyngby, Denmark, where he is currently a Professor Emeritus with the Department of Applied Mathematics and Computer Science. From 1995 to 2010, he was a Provost (Deputy Rector) of DTU. His work includes the analysis of multispectral/hyperspectral and multitemporal data, as well as optical radar sensors. His main research interests include the application of statistics and statistical models in primarily medical image analysis, remote sensing, and industrial applications.

Ernst Krogager (Life Senior Member, IEEE) received the M.Sc. and Doctor Technices (dr.techn.) degrees in electrical engineering from the Technical University of Denmark, Kongens Lyngby, Denmark, in 1981 and 1993, respectively.

He was with the former Danish Defence Research Establishment (DDRE) from 1981 until it was closed in 2006 and merged with the former Air, Army, and Navy Materiel Commands. He is currently a Senior Scientist with Defence Research Centre, Danish Ministry of Defense Acquisition and Logistics Organization (DALO), Ballerup, Denmark. During his doctoral work with DDRE, he conducted experimental and theoretical studies in the area of polarimetric radar imaging, including a stay with Georgia Tech Research Institute (GTRI), Atlanta, GA, USA, from October 1989 until June 1990. During the fall of 1993, he spent three months with NASA Jet Propulsion Laboratory, Pasadena, CA, USA. Since 1984, he has been participating in numerous activities of the NATO Science and Technology Organization (STO—formerly DRG until 1998 and RTO until 2008). Within this community, he chaired research task groups and other activities in the area of radio-frequency-directed energy weapons from 1998 until 2015. He has participated in numerous national and international field trials and led a test campaign in Greenland in 2015 with the F-SAR system of the German Aerospace Center (DLR) for demonstrating the potential of advanced, fully polarimetric synthetic aperture radar (SAR) systems for applications in the Arctic. His current main research interests include the areas of high-resolution polarimetric radar imaging techniques with a focus on the importance of polarimetric information for operational systems.

Henning Skriver (Member, IEEE) received the M.Sc. and Ph.D. degrees in electrical engineering from the Technical University of Denmark (DTU), Kongens Lyngby, Denmark, in 1983 and 1989, respectively.

Since 1983, he has been with DTU, where he is currently the Head of the DTU Space Department. His work has been primarily concerned with topics related to the utilization of SAR data for different applications, such as sea ice parameter retrieval from SAR data, as well as different aspects of land applications of SAR data, such as forestry, agricultural, environmental, and topographic mapping applications using both satellite SAR data and data from polarimetric SARs, e.g., the Danish airborne polarimetric SAR, EMISAR, and the German experimental SAR ESAR. His research interests include methods for the processing of SAR data; SAR image simulation; SAR image filtering; speckle statistics; and texture analysis, segmentation, calibration, change detection, classification, and polarimetric analysis and processing.